Detection of biogenic amorphous calcium carbonate (ACC) formed by bacteria using FTIR spectroscopy

Neha Mehta, Juliette Gaëtan, Paola Giura, Thierry Azaïs, Karim Benzerara

Detection of biogenic amorphous calcium carbonate (ACC) formed by bacteria using FTIR spectroscopy

Neha Mehta[1], Juliette Gaëtan[1], Paola Giura[1], Thierry Azaïs[2], Karim Benzerara[1]*

[1]Institut de Minéralogie, de Physique des Matériaux, et de Cosmochimie (IMPMC), Sorbonne Universités, 75005 Paris, France

[2]Sorbonne Université, CNRS, Laboratoire de Chimie de la Matière Condensée de Paris (LCMCP), F-75005 Paris, France

*Corresponding author

Abstract:

While the formation of intracellular amorphous calcium carbonate (ACC) by living organisms is widespread, its detection in prokaryotes remains difficult owing to its susceptibility to transform or dissolve upon sample preparation. Because of these challenges, a large number of ACC-forming prokaryotes may have been undetected and their abundance in the natural environment is possibly underestimated. This study identifies diagnostic spectral markers of ACC-forming prokaryotes that facilitate their detection in the environment. Accordingly, ACC formed by cyanobacteria was characterized using Fourier transform infrared (FTIR) spectroscopy in near-IR, mid-IR, and far-IR spectral regions. Two characteristic FTIR vibrations of ACC, at ~860 cm^{-1} and ~306 cm^{-1}, were identified as reliable spectral probes to rapidly detect prokaryotic ACC. Using these spectral probes, several *Microcystis* strains whose ACC-forming capability was unknown, were tested. Four out of eight *Microcystis* strains were identified as possessing ACC-forming capability and these findings were confirmed by scanning electron microscopy (SEM) observations. Overall, our findings provide a systematic characterization of prokaryotic ACC that facilitate rapid detection of ACC forming prokaryotes in the environment, a prerequisite to shed light on the role of ACC-forming prokaryotes in the geochemical cycle of Ca in the environment.

Keywords: Amorphous calcium carbonate; FTIR; cyanobacteria; ACC; calcium

1. Introduction

Compared to the crystalline polymorphs of calcium carbonate ($CaCO_3$) such as calcite, vaterite and aragonite, amorphous calcium carbonate (ACC) is more soluble and therefore fairly unstable except in several biotic cases[1]. Biogenic ACC was first documented in eukaryotic organisms such as mollusks, sea urchins, sponges, ascidians, and crustaceans, where ACC acts as a precursor phase for the formation of calcite and aragonite minerals in skeletal architectures [1–6]. Several studies have shown that diverse prokaryotic organisms are also capable of forming ACC. For example, the large uncultured sulfur bacterium *Achromatium oxaliferum*, widely distributed at the oxic-anoxic boundary in sediments of freshwater, brackish, and marine environments, was shown to form numerous intracellular ACC inclusions filling most of the cell volume[7]. Recently, a magnetotactic bacterium affiliated to the Alphaproteobacteria was shown to form intracellular ACC[8]. The repertoire of prokaryotes forming ACC also includes numerous phylogenetically diverse cyanobacteria[9,10]. Detection of biogenic ACC in cyanobacteria was particularly interesting because they are the only known ACC-forming prokaryotes that are culturable in the laboratory. These strains have the highest Ca demand among all cyanobacteria, hypothesized to be driven by their need to form intracellular ACC, which suggests a biological function of ACC. This role possibly consists in an intracellular pH buffer or a storage form of inorganic carbon and/or Ca[11,12]. The formation of ACC by bacteria has significant geochemical implications. First, intracellular ACC inclusions formed by some strains were shown to be associated with their capability to strongly accumulate radioactive alkaline earth elements such as ^{90}Sr and ^{226}Ra, offering some potential for remediating pollutions by these elements[13]. Moreover, some strains of ACC-forming cyanobacteria are shown to sequester high concentrations of alkaline earth elements such as Ba and Sr. This raises questions about the current understanding of the

biological role of Ba/Sr in cyanobacteria and, in reverse, the role of these cyanobacteria in the geochemical cycling of Ba and Sr, especially in environments where they might be abundant[11,14–16]. The biogeochemical implications of bacterial ACC are not only limited to cyanobacteria. Owing to the exceptional size of *A.oxaliferum*, often greater than 17 µm in length and 10 µm in width, ACC within *A. oxaliferum* cells can represent most of the solid calcium present in some sediments [17].

Despite the increasing number of reports about ACC-forming prokaryotes and their biogeochemical significance, detection of ACC in prokaryotes remains a difficult task. Pure abiogenic ACC is highly unstable, transforming within minutes to crystalline calcium carbonate polymorphs such as calcite, or aragonite[18]. In contrast, ACC found in prokaryotes remains relatively stable intracellularly with no obvious spontaneous transformation to crystalline phases such as calcite. The mechanisms underlying such an unprecedented stability of biogenic ACC remain unknown. Various organic or inorganic additives (Mg, P) and/or confinement of ACC within small volumes, have been shown to stabilize ACC [19–22]. This stabilization process is interrupted upon cell lysis, or cell death, which therefore induces ACC loss. Techniques such as scanning electron microscope (SEM) with energy dispersive X-ray spectrometry (EDXS), transmission electron microscope (TEM) with EDXS, and Raman microspectroscopy (but not for ACC in autofluorescent cyanobacteria) have been successfully used to detect ACC in bacteria[23,24] (Table 1). While these techniques are interesting as they provide information at the single-cell scale, their use is time-consuming, which can become prohibitive when several samples (e.g., a screening of numerous bacterial strains) require a preliminary confirmation of the presence or absence of ACC, and when a more global average view of the ACC content of a

sample is needed. Moreover, it has been shown that bacterial ACC can be lost and/or transformed upon some sample preparation protocols (Table 1)[8,23].. Because of these challenges, a large number of ACC-forming prokaryotes may have remained undetected and their abundance in the natural environment possibly underestimated. Overall, there is thus a need for the use of techniques allowing efficient detection of ACC in these complex samples with minimal sample preparation.

Table 1: Summary of techniques used for characterization of ACC in bacteria and their limitations

Technique	Limitation
Scanning electron microscopy (SEM) with energy dispersive X-ray spectrometry (EDXS)[23]	ACC prone to loss upon fixation during sample preparation; time consuming to derive a global average view; no discrimination between crystalline and amorphous phases
Transmission electron microscopy (TEM-EDXS)[23], [8]	ACC prone to loss upon fixation and sample preparation; time consuming to derive a global average view
Raman microspectroscopy[24]	may induce ACC crystallization when using high-intensity lasers; Raman signal is overwhelmed by the auto-fluorescence of ACC forming cyanobacteria

Fourier transform infrared (FTIR) spectroscopy is one of the most commonly used vibrational spectroscopies (e.g.[25–28]), capable of rapidly detecting $CaCO_3$ polymorphs *in situ,* non-destructively, and without complex sample preparation, making it an ideal approach for detection of ACC in prokaryotes at a bulk scale. FTIR spectroscopy has been a popular choice to study the kinetics of ACC crystallization in eukaryotic biominerals (e.g. [2,29]) and abiotic carbonates (e.g. [30–32]). In the mid-IR region, crystalline carbonate phases such as calcite have distinct bands at ~714 cm^{-1} (υ_4), ~866 cm^{-1} (υ_2), ~1084 cm^{-1} (υ_1) and 1420-1470 cm^{-1} (υ_3). ACC shares υ_1- υ_3 vibrations with crystalline $CaCO_3$ but lacks the distinct vibrational band at ~714 cm^{-1} and has an additional shoulder on the υ_3 band [33]. The lack of υ_4 band in ACC along with the characteristic υ_3 shoulder have been used extensively as a diagnostic feature to detect

biogenic ACC present in various eukaryotic carbonates such as spicules of ascidian [6], spicules of sea urchin [29], fish-gut carbonates [34], and earthworm secreted carbonate granules [35]. In eukaryotic carbonates, where crystalline $CaCO_3$ coexists with ACC, the υ_3/υ_4 and υ_2/υ_4 peak intensity ratios have been shown to provide semi-quantitative information on the fraction of amorphous and crystalline phases [18 35]. Unlike the mid-IR spectral range, the far-infrared (FIR) spectral region (80-650 cm^{-1}) offers valuable insights about lower energy lattice vibrations that correspond to vibrations among different carbonate units [36]. Brusentsova et al. compiled a comprehensive dataset of FIR spectra measured on several reference crystalline carbonate polymorphs, but no dataset exists for synthetic or biogenic ACC[37]. While FTIR spectroscopy has been widely used as a tool to detect ACC in eukaryotic carbonates, the application of FTIR spectroscopy to the detection of prokaryotic ACC is limited and not straightforward[38]. Unlike eukaryotic carbonates that are typically composed of a large fraction of crystalline carbonate with ACC and low organic content, prokaryotic ACC consists of a low ACC content mixed with high organic content. Indeed, they are commonly found at low abundance in the environment and surrounded by a complex assemblage of cellular biomolecules [38,39]. The high organic content could mask the characteristic asymmetric vibration (υ_3) band in the region 1500-1400 cm^{-1} and symmetric vibration band (υ_4) at 714 cm^{-1} due to overlapping bands from proteins (amide I and II peaks) and rocking vibration of methylene group of long-chain alkanes [40]. Such interferences may prevent the direct use of diagnostic indicators of ACC (e.g., absence of υ_4 band), previously established based on eukaryotes [39–41]. Mechanically separating the organics from ACC in prokaryotes does not appear as a viable approach as this may result in the rapid transformation of ACC outside the cell, as mentioned previously. Owing to these complications,

the question remains as to what IR spectral features of ACC are suitable for its detection in systems dominated by prokaryotes?

Within this context, we conduct a comprehensive study of the key spectral features of ACC across the near-IR, mid-IR and far-IR, spectral range in ACC-forming cyanobacteria and test these features in a set of cyanobacterial strains whose ACC-forming capabilities remain unknown.

2. Materials and methods

2.1. Synthesis of abiotic ACC

An abiotic amorphous calcium/magnesium carbonate (referred as ACC hereafter) was prepared in-house following the protocol described in[42]. The sample was precipitated by mixing two 100 ml solutions: (i) an aqueous carbonate solution containing 0.05 M of K_2CO_3 (pH = 11.4); and (ii) an aqueous calcium and magnesium solution containing 0.045 M of $CaCl_2.2H_2O$ (Sigma-Aldrich) and 0.053 M of $MgCl_2.6H_2O$ (adjusted to pH = 8.6). The calcium- and magnesium-containing solution was poured directly into the carbonate solution. The resulting precipitate was isolated by centrifugation, washed twice with anhydrous ethanol, and dried at 37°C for 7 days. Bulk mineralogy of the dried powder was analyzed using a Panalytical powder X-ray diffractometer, equipped with a Co-anode X-ray source. Patterns were recorded between 2theta=3-70 degrees, with 0.001 degree steps and 2 milliseconds/step. The characterization of synthesized ACC using X-ray diffraction (XRD) showed only broad peaks, confirming that the synthesis resulted in an amorphous phase (Fig. S1). Synthesized ACC was stored at room temperature in a desiccator. The synthesized ACC remained amorphous for at least 1 year, as

confirmed by XRD (data not shown). Thermogravimetric analysis-differential scanning calorimetry (TGA-DSC) analyses were performed using a SDT Q 600 TA. About 15 mg of powder were placed in an aluminum crucible and the sample was heated up to 900 ^{o}C under a 100 ml-per-minute nitrogen flow. The temperature scan rate was set at 5 ^{o}C per minute. Mass spectrometry analyses were coupled with the TGA-DSC analyses using a ThermoStare GSD 301 T3 (Pfeiffer Vacuum). The signal corresponding to 44 amu (CO_2) and 18 amu (H_2O) were recorded.

2.2. Culture conditions for cyanobacteria strains

Here, we will refer to strains forming intracellular ACC as ACC+ strains and strains not forming intracellular ACC as ACC- strains. Two reference strains, *Synechocystis* PCC 6803 (ACC-) and *Cyanothece* PCC 7425 (ACC+) were cultured in the BG-11 medium, a standard growth medium used for freshwater cyanobacteria and the chemical composition of which is provided in Stanier et al. [43]. Cultures were grown with agitation and continuous light (5-10 µmol m^{-2} s^{-1}). When cell suspensions reached an optical density of ~1, cells were harvested by centrifugation, rinsed, and dried at 40 ^{o}C for 48 hours. In addition, *Microcystis* spp. strains from the Paris Museum Collection (PMC) were included in this study as strains whose capacity to form intracellular ACC was initially unknown. Eight different *Microcystis* strains were cultured to reflect some phenotypic diversity. These strains were grown in the standard BG-11 medium, without agitation, at 23 °C, with a 12:12 photoperiod and a light intensity of ~ 5 µmol m^{-2} s^{-1}. The cells were harvested via centrifugation and dried at 40 ^{o}C for 48 hours. The total Ca concentration of the dried biomass was measured by acid digestion of ~5 mg of dry biomass and subsequent

analysis of the digestate using inductively coupled plasma - optical emission spectrometry (ICP-OES).

2.3 SEM analysis

Microcystis cell suspensions were filtered on 0.22 µm polyethersulfone (PES) filters, then rinsed three times with 10 mL MilliQ® water. The filters were dried at ambient temperature and mounted on aluminum stubs using double-sided carbon tape. The samples were carbon coated prior to SEM analyses. Scanning electron microscopy (SEM) observations were performed using a Zeiss Ultra55 SEM at IMPMC. The electron accelerating voltage used was 10 or 15 kV with a working distance of 7.5 mm and a 60 µm aperture. Images were collected with a backscattered electron detector (AsB detector) and the maps of the different elements (Ca, P, K, Mg, Si, Fe) were retrieved from energy dispersive X-ray spectrometry (EDXS) hyperspectral data (HyperMap).

2.4. FTIR spectroscopy analyses

The abiotic ACC and dried biomass of the different strains were finely ground in an agate mortar. Attenuated total reflectance Fourier transform infrared (ATR-FTIR) spectra were acquired over the mid-IR region (4000-600 cm^{-1}) using a NICOLET 6700 FTIR spectrometer equipped with a diamond internal reflection element (IRE), a KBr beam splitter and a mercury cadmium telluride (MCT) detector. The sample was mounted on the diamond IRE. Spectra were accumulated by collecting 64-100 scans with a resolution of 1 cm^{-1}. Spectra processing including baseline correction, normalization, and peak fit was carried out using the Origin software™. Baseline corrected mid-IR spectra were fitted using a peak analyzer (based on the

Levenberg-Marquardt algorithm). All biomass spectra were fitted in the 945±5 to 845±5 cm^{-1} frequency range. The initial peak position was determined by the local maximum method, which finds the frequency corresponding to the local maximum within the 20-point range. The spectra were fitted with linear combinations of Voigt lineshapes, the centroids of which were initially set to values determined from the local maxima peak analysis and remained unfixed during the fit unless noted otherwise. The baseline was fixed for the fit (cf. section 3.3). The area under the spectrum and above the background was used for spectral normalization (cf. section 3.4).

For the near-infrared analyses, bi-directional reflectance spectra were obtained using the SHADOWS instrument [44] in the 500-4000 nm (20000-2500 cm^{-1}) spectral range. Samples were deposited in a cylindrical sample holder (13 mm in diameter, 5 mm in depth) and measured under a standard observation geometry (incidence=0°, emergence=30°, phase=30°). Spectra were calibrated using the spectral reflectance spectralon™ and infragold™ and corrected for the non-lambertian behavior of spectralon. Last, for far infrared analysis, approximately 6 mg of dried sample were mixed with 80 mg of polyethylene (PE). Pellets were formed in a vacuum press under ten tons of pressure for ~5 min, and spectra were acquired in transmission mode using the Bruker IFS 66v/s FTIR spectrometer in the 600-50 cm^{-1} spectral range, at a resolution of 4 cm^{-1} and using a deuterated triglycine sulfate (DTGS) detector and a multilayer mylar beam splitter. No baseline correction was performed because it was difficult to define and subtract a baseline accurately.

3. Results and Discussion

3.1 Spectral features of synthetic ACC across near-IR, mid-IR and far-IR

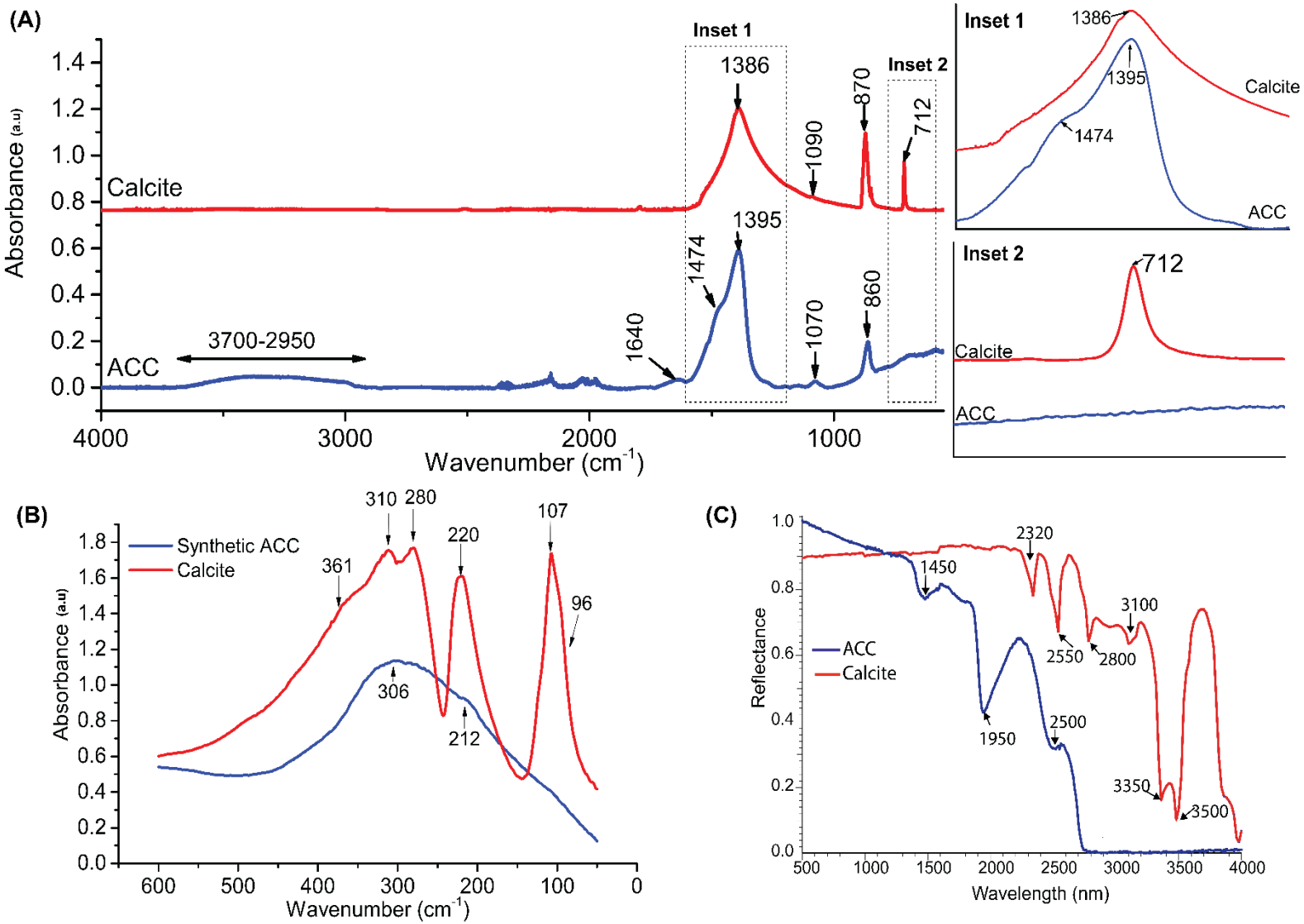

Figure 1: (A) ATR-FTIR spectra of synthetic ACC and calcite in the mid-IR spectral range. The arrows correspond to characteristic mid-IR active frequencies of ACC. The dashed rectangle envelops the zoomed regions of mid-IR ACC spectra shown in the inset 1 (1500-1200 cm^{-1}) and inset 2 (750-680 cm^{-1}). The bands between 2500-2000 cm^{-1} in ACC spectra are due to ambient CO_2 and insufficient purging of the sample chamber. (B) Far-IR spectra of synthetic ACC, and calcite. Arrows denote the characteristic features of ACC and calcite. (C) Near-IR spectra of synthetic ACC, and calcite. Details on the assignment of the vibrations of ACC across the entire region are listed in Table S1. The X-axis is in wavelength, where 500 nm corresponds to 2x 10^4 cm^{-1} and 4000 nm corresponds to 2.5 x 10^3 cm^{-1}.

The characteristic peaks of synthetic ACC across the spectral range of 20,000-50 cm^{-1} are shown in Fig. 1 and summarized in Table S1. The band assignments of the IR peaks observed in ACC are listed in Table S1. In the mid-IR spectral region, ACC is specifically indicated by the presence of a shoulder at 1474 cm^{-1} and the absence of a peak at 712 cm^{-1} (Fig. 1, Inset 1-2)[32]. This spectral range also showed for ACC a broad band between 2950 and 3700 cm^{-1} (O-H stretching) and at 1650 cm^{-1} (O-H bending), both corresponding to structural water within ACC[32]. Consistently, the water content in ACC was estimated to 17 wt% (corresponding to 0.94 mole of water per carbonate) based on TGA-DSC-MS analyses (Fig. S2). The out-of-plane bending absorption (U_2) at ~860 cm^{-1} (FWHM=25 cm^{-1}) was observed. This band is sensitive to differences in chemical environment changes from amorphous to crystalline forms [30]. Indeed, with the transformation of an amorphous phase to a crystalline phase, the U_2 band position shifts from 860 cm^{-1} (ACC) to 870 cm^{-1} (calcite) (Fig. 1A). The U_2 band position is also sensitive to the Mg content in ACC: the band shifts towards lower wavenumbers with increasing Mg content in ACC and can vary between 860-864 cm^{-1} [20,27]. The remaining bands in the mid-IR spectral range were characteristic vibrations of the carbonate ion and are common in both ACC and crystalline polymorph[32].

In the FIR region, ACC shows a broad peak around ~306 cm^{-1} and a weak shoulder on this broad peak at ~212 cm^{-1} (Fig.1B). For comparison, calcite FIR spectra show several sharp peaks at 310 (with a shoulder at 361), 280, 220, 107 (shoulder at 96) cm^{-1}, consistent with previous studies (e.g. [36,37]). These sharp bands are due to IR-active collective lattice vibrational modes that involve relative translations of the calcium and carbonate ions. In contrast, ACC is rotationally disordered which results in a broad envelope across the available frequencies [45]. Lastly, in the

NIR region, the ACC spectra is dominated by broad absorption peaks at 1450 nm (6896 cm^{-1}), 1950 nm (5128 cm^{-1}), 2500 nm (4000 cm^{-1}), and the absence of absorption bands beyond ~2500 nm (Fig. 1C). The peaks <2500 nm are attributed to O-H stretching overtones originating from structural and/or weakly bonded water[46]. Above 2500 nm the reflectance is close to zero, because of the saturation of the fundamental OH stretching mode. Moreover, the typical carbonate vibrations in region >2500 nm (see calcite NIR spectra in Fig. 1C) are masked by strong water-related absorption bands in ACC [47,48] [49]. Overall, due to the presence of water in ACC, the NIR region offers no diagnostic spectral features of ACC.

Several key insights can be drawn from the above analyses. All bands of ACC in the NIR region are masked by structural water. Almost all biological occurrences of ACC are known to be hydrous, and thus, NIR is not a particularly useful IR fingerprinting region for ACC. In contrast, mid-IR and far-IR regions offer promising diagnostic spectral features that we test below to detect ACC in cyanobacteria.

3.2 FTIR spectra of ACC+ and ACC- –cyanobacteria in the mid-IR and far-IR ranges

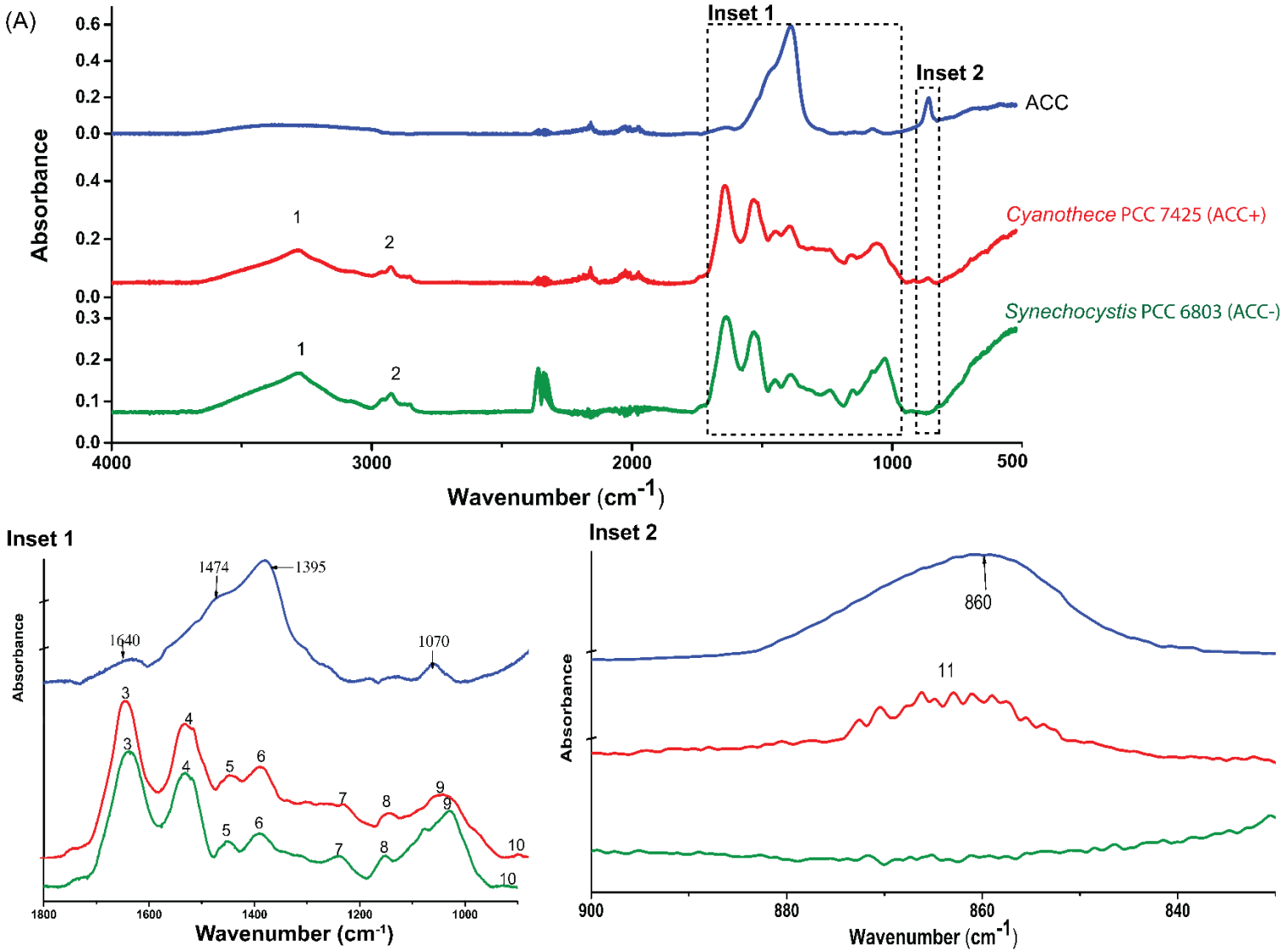

Figure 2: (A) ATR-FTIR spectra of the *Cyanothece* PCC 7425 (ACC+), *Synechocystis* PCC 6803(ACC-), and synthetic ACC. The bands between 2500-2000 cm^{-1} in the spectra are due to ambient CO_2 and H_2O resulting from insufficient purging of the sample chamber. The dashed rectangle envelops the zoomed regions of mid-IR ACC spectra shown in the inset 1 (1800-900 cm^{-1}) and inset 2 (900-820 cm^{-1}). Numbers on the spectra correspond to the band# in Table 2.

Several absorption bands were identified in the mid-IR spectra of *Cyanothece* PCC 7425 (ACC+) (Fig. 2). The spectral band assignment for the ACC+ and ACC- strains was achieved based on a comparison and cross-referencing against existing FTIR literature about photorophic microorganisms ([41,50–53]) and is summarized in Table 2. Bands [1-10] were present in both *Cyanothece* PCC 7425 and *Synechocystis* PCC 6803 and were attributed to non-ACC components. These components included O-H vibrations derived from water (band 1), methyl and methylene group vibrations from lipids and fatty acids (band 2), amide I and amide II from proteins (bands 3,4), asymmetric bending of methyl groups of lipids, and symmetric stretching from C-O group in carboxylic acids (bands 5,6), a combination of asymmetric stretching from P=O group of nucleic acids and/or polyphosphates and C-O stretching vibrations from polysaccharides (bands 7, 8, 9, 10) [50,51,54]. The bands between 2500-2000 cm^{-1} are due to ambient CO_2 and insufficient purging of the sample chamber. *Cyanothece* PCC 7425 had an additional absorption band present at ~860 cm^{-1} (band 11) which was absent in *Synechocystis* PCC 6803. The peak position of band 11 coincides with the ACC peak at 860 cm^{-1} (Fig. 2). Moreover, the FWHM of the fitted peak at 860 cm^{-1} in *Cyanothece* PCC 7425 was 25.1 cm^{-1}, matching that of the 860 cm^{-1} peak of ACC. No absorption band was found around ~700 cm^{-1} region in *Cyanothece* PCC 7425 suggesting the absence of crystalline carbonate polymorphs. This is consistent with the under-saturation of the BG-11 growth medium with respect to carbonate phases, which does not allow the precipitation of extracellular crystalline carbonates in the growth solution (Fig. S3). Spectral features of ACC apart from the 860 cm^{-1}, namely 3600-2700 cm^{-1} (O-H stretching), 1650 cm^{-1} (O-H bending), 1470-1420 cm^{-1} (υ_3) and 1084 cm^{-1} (υ_1) had strong interference with the lipids and water bands (1, 2), protein bands (3, 4), carboxylic

266 acids bands (5,6) and nucleic acid or phosphorylated polysaccharides (7,8,9) as shown in Fig.
267 2B.

268

Table 2: Wavenumbers and band assignment for characteristics vibrations found in the mid IR spectra of *Cyanothece* PCC 7425 and *Synechocystis* PCC 6803. The band assignment was primarily based on the [50,51,54].

Band Index	Wavenumbers (cm^{-1})	Main functional group
1	3279	water
2	2960-2856	methyl and methylene group vibrations from lipids and fatty acids
3	1641	amide I from proteins
4	1528	amide II from proteins
5	1444	methyl groups of lipids and C-O group in carboxylic acids
6	1391	methyl groups of lipids and C-O group in carboxylic acids
7	1241	Nucleic acids, phosphoryl group
8	1153	P=O group of nucleic acids and/or polyphosphates and C-O vibrations from polysaccharides
9	1058-1029	P=O group of nucleic acids and/or polyphosphates and C-O vibrations from polysaccharides
10	919	P=O group of nucleic acids and/or polyphosphates and C-O vibrations from polysaccharides
11	860	out-of-plane bending of carbonates in ACC (υ_2)

269

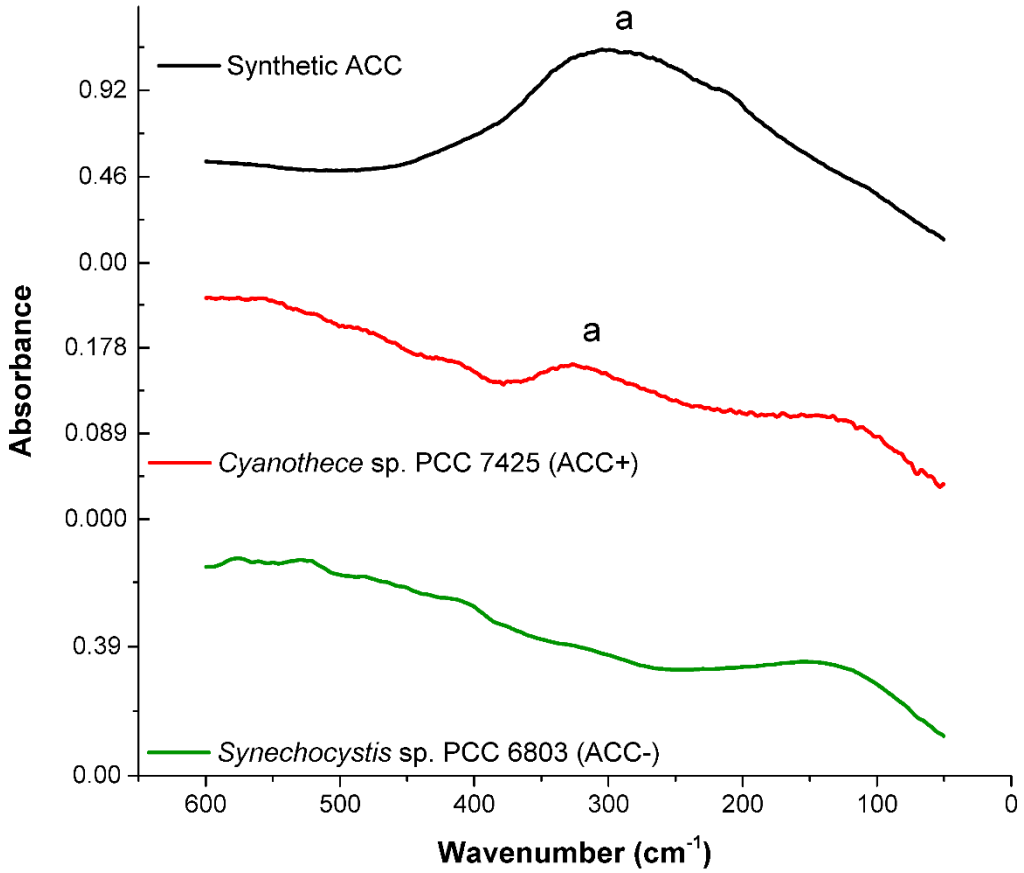

Figure 3: FIR spectra of the ACC+ and ACC- cyanobacteria. The peak labeled marked as "a" denotes the location of the characteristic features of ACC in FIR at ~306 cm^{-1}. This peak was at ~320 cm^{-1} in *Cyanothece* PCC 7425 (ACC+).

In the NIR region, the spectra of *Cyanothece* PCC 7425 and *Synechocystis* PCC 6803 looked almost identical, which is not surprising based on the lack of ACC features in the NIR region due to superimposition with structural water (Fig. S4). The different peaks found in the NIR spectra of cyanobacteria were primarily attributed to lipids, proteins, and water (Fig. S5) in accordance to Vaidyanathan et al.[55].

In the FIR region, broad features around 150 cm^{-1} were observed in both ACC+ and ACC- cyanobacteria strains, possibly corresponding to torsional frequencies of primary amines[56,57].

278 Interestingly, FIR spectra of *Cyanothece* PCC 7425 showed a broad but strong peak around ~320
279 cm^{-1}, which was absent in *Synechocystis* PCC 6803 (Fig. 3). The asymmetric line shape is
280 characteristic for samples prepared with PE as filling material, and it is not found in the spectra
281 of samples prepared without PE [58]. The position of this peak coincides with the broad peak
282 observed in FIR spectra of synthetic ACC (Fig. 1), suggesting that the peak might be due to ACC
283 in *Cyanothece* PCC 7425.

284 Comparing the mid-IR and far-IR spectra of ACC+ and ACC- cyanobacteria strains,
285 only the υ_2 band at 860 cm^{-1} and the broad peak at ~306 cm^{-1} (characteristic vibrations of ACC)
286 are free from overlaps with spectral features attributed to organics. Consistently, they are present
287 in ACC+ cyanobacteria, while absent in ACC- cyanobacteria. Indeed, ACC features in spectral
288 region >900 cm^{-1} are masked by vibrations from organics, suggesting that spectral features of
289 ACC in the spectral region > 900 cm^{-1} are not reliable diagnostic indicator of presence of ACC
290 in a sample dominated by organics. Such complex combination between ACC bands and organic
291 bands is shown to be absent in organic-poor eukaryotic ACC, where the intense vibrational
292 bands from ACC mask the bands from the matrix biomolecules, making the ACC mid-IR bands
293 in regions > 900 cm^{-1} detectable[59]. Based on these results, we argue that the use of spectral
294 features of ACC in region > 900 cm^{-1} to confirm ACC in an organic-rich matrix could result in
295 some misleading results. For instance, Enyedi et al. used the presence of bands at 1494 cm^{-1} and
296 at 1066 cm^{-1} in an organic-rich bacterial extra-polymer-substance (EPS) to infer the presence of
297 ACC in bacterial EPS[38]. Fortunately, this interpretation was further supported by other
298 complementary techniques (electron diffraction and Raman spectroscopy). However, we note
299 that the interpretation of the FTIR data by Enyedi et al. is not accurate, since the characteristic

peaks of ACC at 1494 cm^{-1} and at 1066 cm^{-1} could be attributed to the vibrations from organic components present in the samples, such as proteins, nucleic acid, and phosphorylated polysaccharides.

Whether these spectral features apply to a broader diversity of prokaryotes remains an open question. The characteristic peaks of major biomolecules (e.g., proteins, polysaccharides) can be expected to remain the same across different prokaryotic taxa, but some minor differences have been reported due to solution chemistry, growth conditions and taxonomy[41,60–62]. In the next section, we assess the effect of physiological differences on the above-identified ACC spectral features by surveying different cyanobacterial strains affiliated to the same *Microcystis* genus.

3.3 Case study: Examining the capability of *Microcystis* strains to form ACC using FTIR spectroscopy and SEM

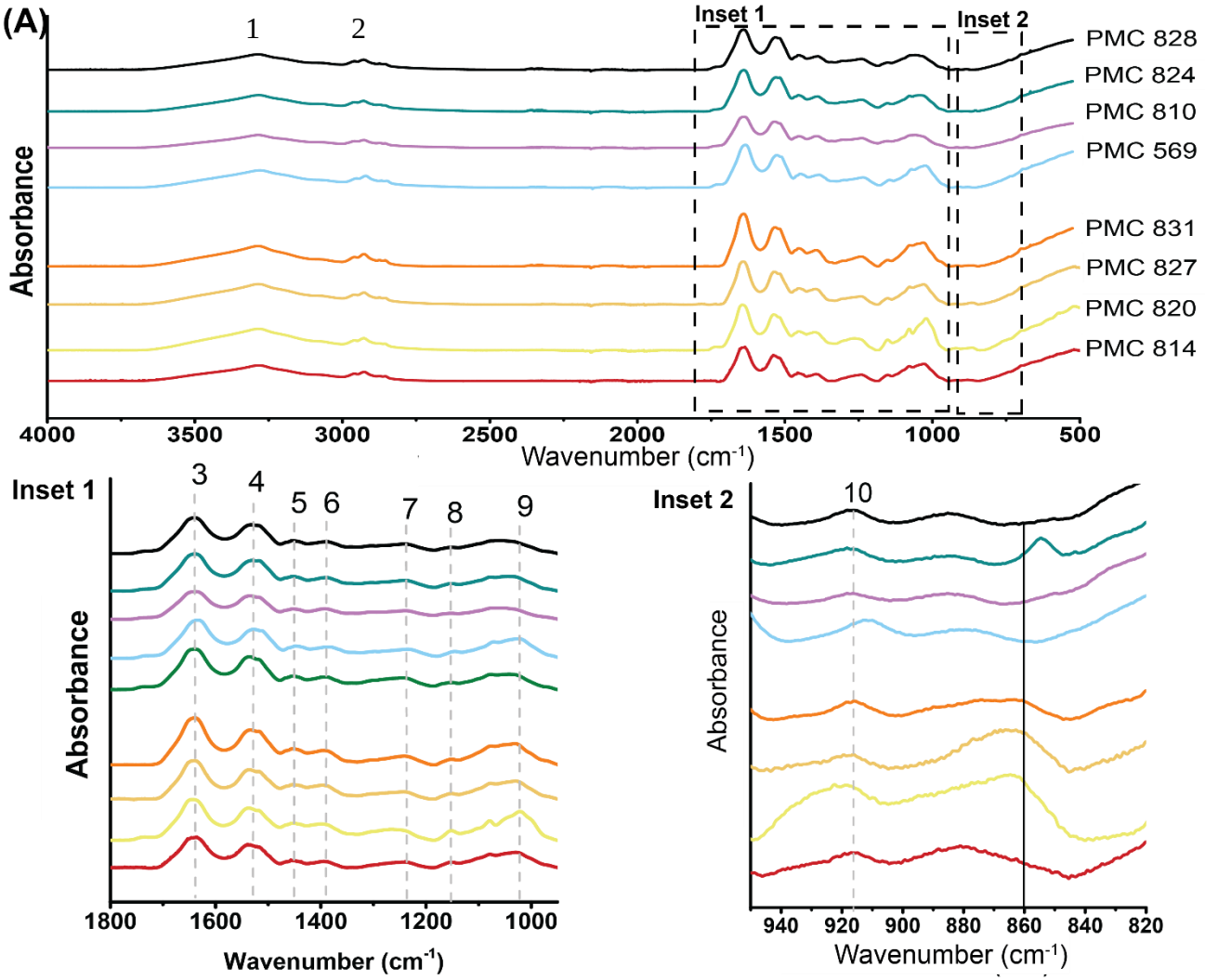

Figure 4: (A) ATR-FTIR spectra of PMC *Microcystis* sp. strains in the mid IR range. The dashed rectangle envelops the zoomed regions of mid-IR ACC spectra shown in the inset 1 (1800-900 cm^{-1}) and inset 2 (950-820 cm^{-1}). Numbers on the spectra correspond to the band numbers and their assignment are provided in Table1. The vertical gray dash lines in Inset 1 are guidelines to facilitate identification of the position of bands (1-10) in the different PMC *Microcystis* sp. strains. The solid black line in Inset 2 denotes the location of characteristic U_2 band of ACC (~860 cm^{-1}).

316 The cyanobacterial genus *Microcystis* has been intensely[e.g.63–66] studied because it
317 comprises some strains producing hepato- and neuro-toxins, and blooming mostly in freshwater
318 and brackish water, causing significant environmental issues.

319

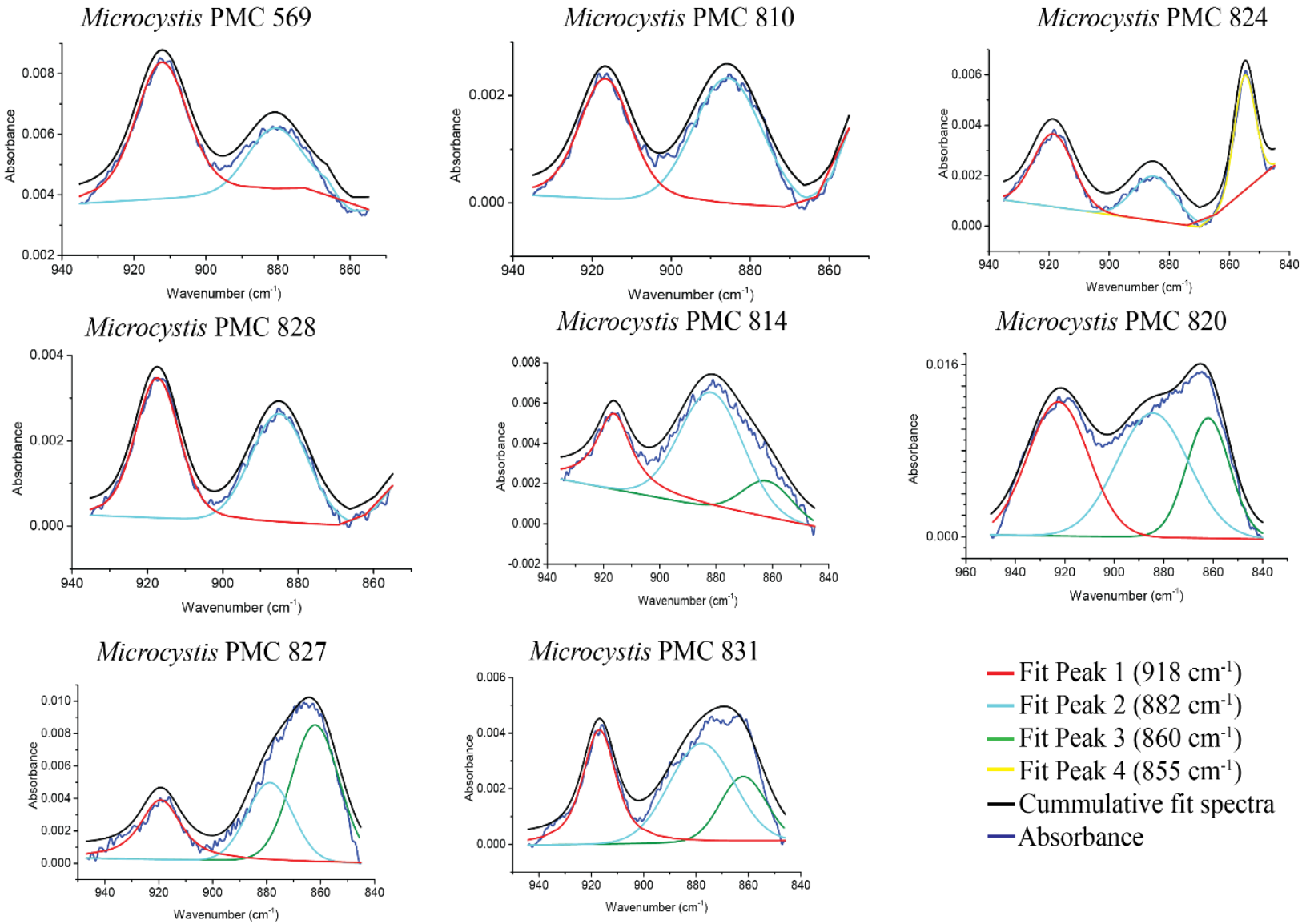

Figure 5: Peak fit of *Microcystsis* strains in the frequency region 940-840 cm^{-1}. For strains PMC 569, PMC 810 and PMC 828, best fit was achieved by using 2 band components (~918 cm^{-1}, 882 cm^{-1}); for PMC 824, best fit was achieved by using 3 band components (918 cm^{-1}, 882 cm^{-1} and 855 cm^{-1}); for strains PMC 814, 820 and 831, 3 band components (918 cm^{-1}, 882 $cm^{-1}$and 860 cm^{-1}) yielded best fit. The peak positions of the fitted bands are noted in table 3 and fit quality summarized in the table S2

While ACC formation has been evidenced in a broad diversity of cyanobacteria [10], *Microcystis* has so far been poorly studied in this perspective. Here, we acquired FTIR spectra of several different *Microcystis* strains in the mid-IR region to investigate if some of them may form ACC (Fig. 4). Characteristic bands of proteins, lipids, polysaccharides, and phosphate groups (bands 1-10) were observed in the 4000-900 cm^{-1} spectral region in all *Microcystis* strains, similarly to what was observed in *Cyanothece* PCC 7425 and *Synechocystis* PCC 6803 (Fig. 4A). The band location and assignment were in good agreement with the previously reported bands in *Microcystis* in the 4000-1000 cm^{-1} frequency range[41]. Visual inspection of *Microcystis* strains in the 950-800 cm^{-1} region reveals that all *Microcystis* spectra had a clearly defined band at ~918 cm^{-1}, labeled as band 10 in Fig. 4C. Additionally, a broad peak at ~880 cm^{-1} was clearly observed in *Microcystis* PMC 569, PMC 810, PMC 824, and PMC 828, while this band appeared visually as an asymmetric broad band for the other *Microcystis* strains (PMC 814, PMC 820, PMC 827 and PMC 831) (Fig. 4C). A sharp peak at ~855 cm^{-1} was observed in *Microcystis* PMC 824 only. In *Microcystis* PMC 820, PMC 827 and PMC 831, a band close to 860 cm^{-1} was observed. Unlike what was observed for *Cyanothece* PCC 7425, this band, possibly affiliated to the 860 cm^{-1} peak of ACC, was not well-defined and overlapped with other neighboring peaks in the 950-800 cm^{-1} spectral range (Fig. 4B).

To overcome the challenge of overlapping bands, we fitted the experimental spectra of all *Microcystis* strains in the 950-800 cm^{-1} frequency range with a combination of four (Voigt) peak components: fit peak 1 at ~918 cm^{-1} and fit peak 2 at ~880 cm^{-1}, fit peak 3 at ~860 cm^{-1}, and fit peak 4 at ~855 cm^{-1}. Fig. 5 shows the best fits for different *Microcystis* strains, and the peak properties are listed in table 3. The fit quality parameters are listed in Table S2. Based on the

curve fit, we find that fit peak 1 at ~918 cm^{-1} and fit peak 2 at ~880 cm^{-1} were present in all *Microcystis* strains (Table 3). The fit peak 1 at ~918 cm^{-1} was also present in *Synechocystis* PCC 6803 and *Cyanothece* PCC 7425 (peak labeled 10 in Fig. 2 and Fig. 4) and is attributed to a combination of asymmetric stretching from the P=O group of nucleic acids and/or polyphosphates and C-O stretching vibrations from polysaccharides. Intra-strain variations in the intensity of fit peak 1 at ~918 cm^{-1} could potentially be due to variations in the polyphosphate and polysaccharide content of the cells. Polyphosphates and polysaccharides serve as carbon, phosphorus and energy reserves, and their content is known to vary during the growth of the cyanobacteria [41,52]. The fit peak 2 at ~880 cm^{-1} could match with vibrations of crystalline carbonates. However, no peak at ~714 cm^{-1} was found suggesting the absence of such phases. Alternatively, fit peak 2 may be assigned to bicarbonate[67]. Cyanobacteria are known to accumulate high amount of intracellular bicarbonate owing to carbon concentrating mechanisms[68]. The bicarbonate band is generally weak and sensitive to the degree of hydration of bicarbonate ions, i.e. the band is red shifted and becomes broader with increasing hydration [69]. Unfortunately, it is not possible to further confirm this band assignment based on other bands characteristic of bicarbonate since they overlap with carbonate vibrations and/or are masked by vibrations of biomolecules. A third possible affiliation of fit peak 2 can be made as strong =C-H out-of-the plane bending vibrations of alkenes [54]. The other peaks characteristics of alkenes are stretching =C-H vibrations at 3100-3000 cm^{-1} and C=C stretching vibrations at 1660-1500 cm^{-1}, both of which overlap with band #1 (attributed to water) and band #3, #4 (attributed to proteins) in all *Microcystis* strains[70]. Alkenes typically form part of the structure of fatty acids, and/or carotenoid pigments (commonly present in photosynthetic cells and one of the main components

of the phytoaccumulation complex[70,71]). Last, fit peak 2 at ~880 cm^{-1} could be due to the P=O group vibrations of polyphosphates as proposed by Wang et al. [72]. This assignment is also consistent with the presence of other characteristic bands (bands 7, 8, 9, 10) of polyphosphates observed in all the *Microcystis* strains (Table 2). As a summary, fit peak 2 may result from vibrations in bicarbonates, alkenes and/or polyphosphates. Interestingly, fit peak 4 at 855 cm^{-1} was only found in *Microcystis* PMC 824 and had a relatively narrow FWHM (8 cm^{-1}) in comparison to the 860 cm^{-1} (U_2) band of ACC (FWHM=25 cm^{-1}) suggesting that the band at 855 cm^{-1} is not linked to the 860 cm^{-1} band of ACC. Nitrates and chloride salts, contained by the BG-11 growth medium are known to give rise to a sharp peak at ~855 cm^{-1}[73]. Thus, the band at ~855 cm^{-1} could be assigned to nitrate salts from the growth medium and may result from in-sufficient rinsing of the *Microcystis* PMC 824 cell suspension.

Last, peak fit of the *Microcystis* spectra revealed that fit peak 3 at 860 cm^{-1} was only present in strains PMC 814, PMC 820, PMC 827, and PMC 831 (Fig. 5 and Table 3). The overall quality of the fit for these strains was poorer when fit peak 3 was not included in the fit components (Fig. S5 and Table S2). The FWHM of fit peak 3 at 860 cm^{-1} in *Microcystis* strains was slightly narrower (~ 21 cm^{-1}) but still comparable with the 860 cm^{-1} band of synthetic ACC (25 cm^{-1}) (Table 3). By contrast, poor fit quality was obtained upon fitting a band at 860 cm^{-1} in the experimental spectra of the PMC 824, PMC 569, PMC 810, and PMC 828 strains, suggesting that the band at 860 cm^{-1} was not present in these spectra (Fig. S5 and Table S2). Thus, based on the presence/absence of the 860 cm^{-1} band in *Microcystis* strains, we were able to screen four (PMC 814, PMC 820, PMC 827 and PMC 831) out of eight strains as promising candidates to possess ACC-forming capabilities. These findings were further reinforced by analyzing the FIR

region spectra of *Microcystis* strains. We compared the FIR spectra of two *Microcystis* strains: *Microcystis* PMC 827 and *Microcystis* PMC 824. We found broad features around 150 cm^{-1} in both PMC 827 and PMC 824 strains, similar to that observed in ACC+ and ACC- cyanobacterial strains and possibly corresponding to torsional frequencies of primary amines[56,57]. FIR spectra of *Microcystis* PMC 827 showed a broad but strong peak around ~320 cm^{-1}, which was absent in *Microcystis* PMC 824 (Fig. 6). The position of this peak coincides with the broad peak observed in FIR spectra of synthetic ACC as well as in ACC+ forming cyanobacteria strain (Fig. 3), confirming the presence of ACC in *Microcystis* PMC 827 and its absence in PMC 824. This is consistent with observations on the ACC-forming potential of these strains derived from the mid-IR spectra of these strains.

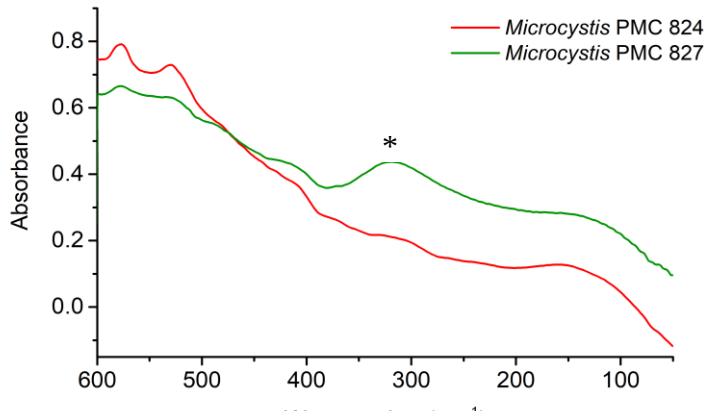

Figure 6: FIR spectra of *Microcystis* PMC 827 and *Microcystis* PMC 824. The peak labeled marked as "*" denotes the characteristic features of ACC in FIR at ~300-320 cm^{-1}.

401

402 Table 3: Peak spectral properties of the fitted peaks in *Microcystis* strains corresponding to the best fit for

403 each strain.

	Fitted Peak Centers (cm^{-1})				FWHM (cm^{-1})			
	Peak 1[*]	Peak 2	Peak 3[**]	Peak 4	Peak 1	Peak 2	Peak 3[ⁿ]	Peak 4
Microcystis PMC 569	912[ı]	881±0.09	‴	NA	18±0.19	17±0.11	‴	‴
Microcystis PMC 810	917[ı]	886±0.06	‴	NA	16±0.16	20±0.73	‴	‴
Microcystis PMC 824	919[ı]	885±0.1	‴	855±0.03	16±0.15	17±0.22	‴	8±0.06
Microcystis PMC 828	917[ı]	885±0.04	‴	‴	14±0.08	18±0.09	‴	‴
Microcystis PMC 814	916[ı]	882±0.71	862±1.77	‴	15±0.82	26±1.14	21±1.19	‴
Microcystis PMC 820	923[ı]	884±1.19	862±0.3	‴	29±1.14	34±4.4	21±1.45	‴
Microcystis PMC 827	919[ı]	879±3.07	862±1.8	‴	18±0.61	20±4.27	21±0.92	‴
Microcystis PMC 831	917[ı]	878±5.88	862±2.6	‴	15±0.91	29±8.4	21±1.78	‴

[*]This fit band is same as band 10 in table 1

[ı] This parameter was fixed

[**]Peak 3 center was constrainted to vary between 861± 1 cm^{-1}

[ⁿ] The gaussian FWHM of peak 3 was set to be at least 20 cm^{-1}

404 ‴ No peak fit at this location.

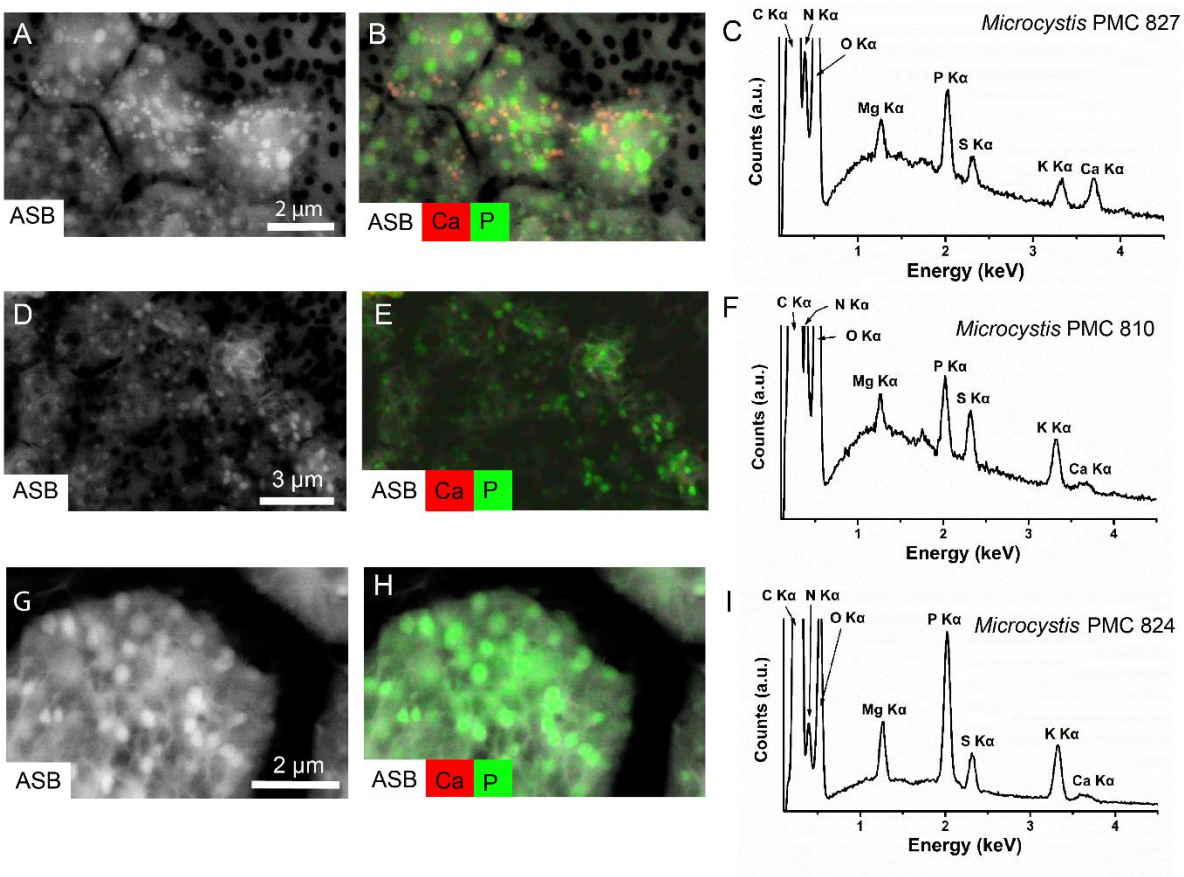

Figure 6: Representative SEM images of *Microcystis* strains found to be capable of forming ACC and not forming ACC based on FTIR. (A, D, G) SEM image of the *Microcystis* PMC 827 (ACC+), *Microcystis* PMC 810 (ACC-), *Microcystis* PMC 824 (ACC-) strains in AsB detection mode, respectively. (B, E, H) Corresponding overlay of AsB image with EDXS maps of Ca (red) and P (green) for *Microcystis* PMC 827 (ACC+), *Microcystis* PMC 810 (ACC-), *Microcystis* PMC 824 (ACC-) respectively. (C, F, I) SEM-EDXS spectra of *Microcystis* sp. PMC 827 (ACC+), *Microcystis* PMC 810 (ACC-), *Microcystis* PMC 824 (ACC-) respectively.

To further confirm our findings on the capability of *Microcystis* strains to form ACC, we analyzed all the *Microcystis* strains by SEM-EDXS (Fig. 6 and Fig. S6). For each strain, several cell aggregates were randomly selected, and EDXS maps were obtained. Each cell had a variable number of inclusions, ranging from zero to a hundred. Based on EDXS elemental mapping, all *Microcystis* strains contained inclusions enriched in P, containing Mg, K, and Ca were interpreted as polyphosphate (polyP) granules. Several functions of polyP inclusions have been

inferred in bacteria, including the provision of an alternative source of energy under some specific environmental conditions[10]. Observation of polyP inclusions in *Microcystis* is consistent with the presence of polyP IR bands [8-10] in all *Microcystis* strains [Table 2, Fig. 4]. Qualitatively, the number of polyP inclusions vary among different *Microcystis* strains as observed in SEM micrographs, which suggests that the amount of polyP content varies across *Microcysits* strains (Fig. 6 and Fig. S6). The variation in polyP content across *Microcystis* strains is also reflected in the differences observed in peak height of the polyP bands [8-10] present in *Microcystis* strains (Fig. 4). In contrast to polyP inclusions, inclusions enriched in Ca with little or no P were interpreted as ACC. They were only found in strains PMC 814, 820, 827, and 831, which was perfectly consistent with FTIR results. Altogether, based on the presence/absence of the mid-IR U_2 absorption band at 860 $cm^{-1}$and a broad band at ~300 cm^{-1} in FIR region, both characteristics of ACC, and using SEM-EDXS as a supporting tool, we identify four out of eight *Microcystis* strains that are able to form ACC, whereas the rest of the *Microcystis* strains do not form ACC, at least not in sufficient amount to be detected by FTIR spectroscopy and/or under the growth conditions that were used in the present study.

Semi-quantitative estimation of ACC in *Microcystis*

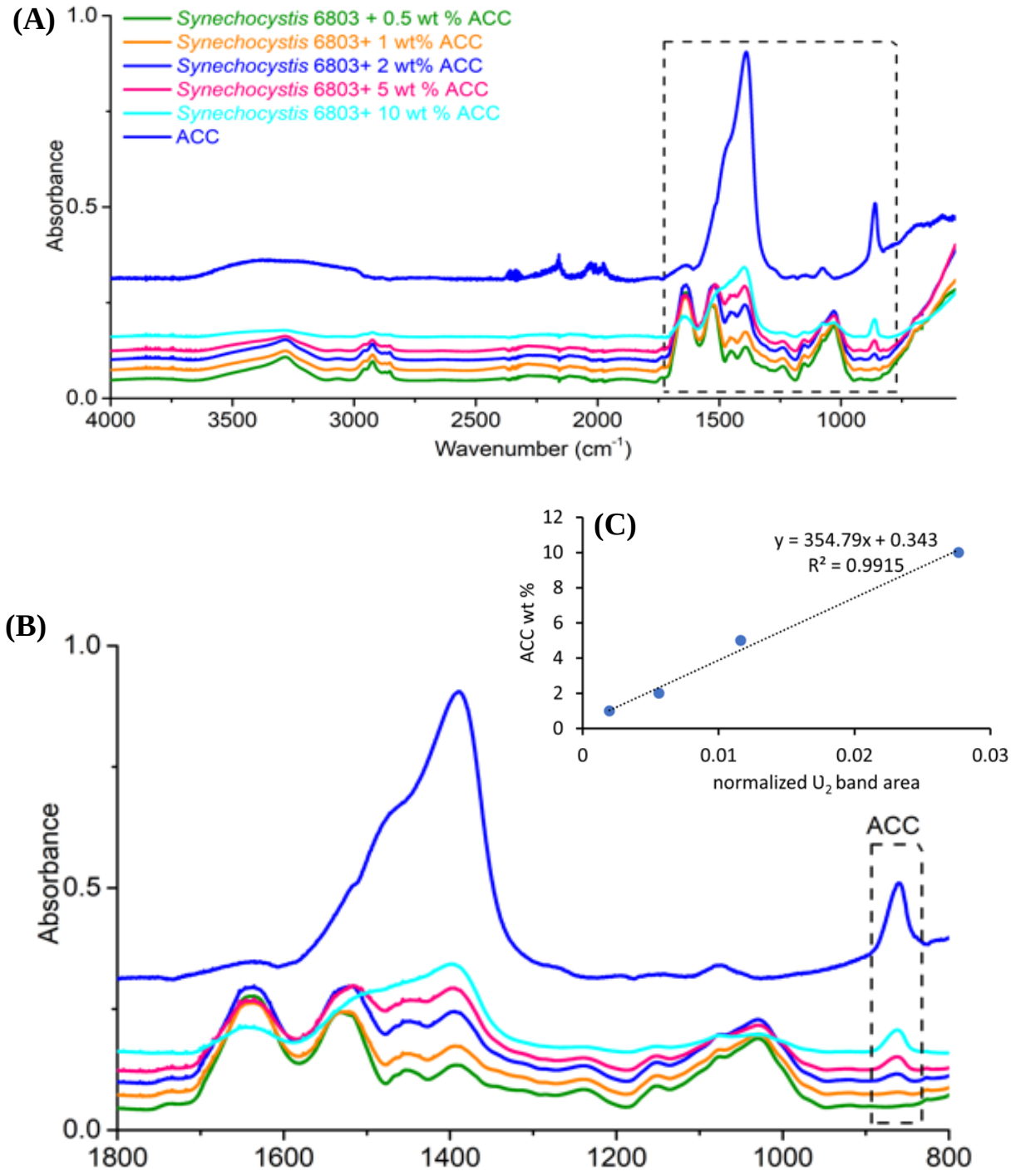

Figure 7: (A) ATR-FTIR spectra of *Synechocystis* PCC 6803-ACC mixtures. (B) Zoomed plot of the boxed region in (A). The peak intensity of U_2 band of ACC was normalized by the frequency region marked by dashed rectangle in (A). (C) The FTIR calibration curve of normalized peak area of U_2 band for different *Synechocystis* PCC 6803-ACC mixtures.

429

The relative intensity of FTIR spectral bands such as proteins, silicate, lipids have frequently been used to correlate the chemically measured content of cellular biomolecules [74,75]. In this study, the intensity of the 860 cm^{-1} band is used to compare the variation in ACC content in *Microcystis* strains identified as ACC+ strains. To do so, we first measured a calibration curve to assess the relationship between ACC wt % in a physical mixture of *Synechocystis* PCC 6803 (ACC-) +synthetic ACC and the normalized 860 cm^{-1} band area. Mid-IR spectra of different *Synechocystis* PCC 6803 +synthetic ACC mixtures are shown in Fig. 7A. The higher the ACC wt % in the mixtures, the lower the contribution of the organics to the characteristic ACC bands at 1474 (U_3), 1070 (U_1), and 1640 (O-H bending) was observed (Fig. 7B). An increase of the ACC content in the mixtures correlated with an increase of the 860 cm^{-1} band (Fig. 7B). To correct for possible variations in the path length (thickness of individual cyanobacterial mixture), and water content, all spectra were area-normalized. In the literature, the integrated area under the amide I/II band has been used for normalizing diverse peak areas of interest[76]. However, for the different mixtures of the present study, the relative absorption was not constant for both amide I and II bands (Fig. 7B). Moreover, amide bands suffer from interferences with vibrations associated with ACC structural water (O-H bending at 1650 cm^{-1}) and the U_3 band of ACC at 1474 cm^{-1} (Fig. 7B). Therefore, in our study, it was more appropriate to use the integrated area between 1800-832 cm^{-1} frequencies, to normalize the area under the 860 cm^{-1} band (between 880-832 cm^{-1}). The computed changes in the normalized area of the peak at 860 cm^{-1} are plotted against the ACC wt % in the mixtures (Fig. 7C). A strong linear correlation is found between the normalized area of the 860 cm^{-1} band and the amount of ACC present in the *Synechocystis* PCC 6803 + ACC mixtures. We applied this relationship to estimate the ACC content in ACC+

452 *Microcystis* strains. As shown in Table 4, the "calculated ACC" content in ACC+ *Microcystis*
453 strains varied between 0.5-3% wt ACC (Table3). This calculated ACC content was compared

Table 4: The calculated ACC (wt %) content in 4 *Microcystis* strains, using the calibration curve equations determined on artificial *Synechocystis* PCC 6803 -ACC mixtures.

Strain	Normalized U_2 band area	Calculated ACC (wt%)	Derived ACC content*
PMC 814	4.00E-04	0.48	0.91
PMC 820	8.00E-03	3.18	4.23
PMC 827	2.38E-03	1.19	3.92
PMC 831	7.20E-04	0.60	

* Derived based on the assumption that the total Ca concentration measured on ICP-OES in the sample constitutes ACC reservoir.

454

455 with the ACC content estimated from the measured total Ca concentration in the dried biomass,
456 referred to as the "derived ACC content" in Table 4. Although the estimated absolute value of
457 derived and calculated ACC content in strains were different, the trends were similar, that is
458 *Microcystis* PMC 820 had the highest ACC content, followed by *Microcystis* PMC 827. Similar
459 variations in the ACC content of diverse strains have been observed before. For the known
460 ACC+ cyanobacteria strains, the maximum amount of ACC content can vary from 2-8 wt%[11].
461 Reasons for such variations in the ACC content are not clear and will need to be further assessed
462 by future studies. It could be linked with the varying physiological state of the cells, or a
463 different function of ACC in these strains[10,11].

464 **Conclusions**

465 This study probed intact cells of cyanobacteria forming intracellular ACC inclusions using FTIR
466 spectroscopy, to identify diagnostic IR spectral features of ACC that are suitable for its detection
467 in systems dominated by prokaryotes. ACC has several IR active bands that have been widely
468 used to discriminate ACC from other $CaCO_3$ polymorphs. While several of these bands were

found to overlap with characteristic bands of proteins, lipids, polysaccharides, and phosphate groups, two ACC characteristic bands at 860 cm^{-1} and a broad peak at ~306 cm^{-1} were free from any overlap from biomolecules. Moreover, the bands at 860 cm^{-1} and a broad peak at ~306 cm^{-1} were systematically present only in ACC+ cyanobacteria and absent in ACC- cyanobacteria, suggesting that both bands could serve as a spectral marker to screen strains for their capability of forming ACC. The reliability of these diagnostic features of ACC was tested on several *Microcystis* strains whose ACC-forming capabilities were unknown. Using mid-IR and far-IR ACC spectral features, we identified four out of eight *Microcystis* strains as ACC forming strains. These findings were confirmed by SEM-EDXS observations. Lastly, we quantified the ACC content of *Microcystis* strains using the variations in 860 cm^{-1} band intensity. While the semi-quantification approach used here is an approximation, it provides some insights into assessing the Ca accumulation potential of the ACC-forming *Microcystis* strains and other prokaryotes and their relevance as a geochemical reservoir of Ca in the environment. Overall, FTIR spectroscopy in the mid-IR and far-IR range appear as a very valuable and reliable tool to diagnose the presence of ACC in bacteria and screen efficiently numerous samples before using more time-consuming techniques such as electron microscopy. Whether these spectral features are effective in detecting ACC−forming prokaryotes in a complex environmental sample composed of different microbial populations as well as extracellular minerals remains an interesting topic for future research.

Acknowledgments

We would like to thank the financial support from the Institut de science des matériaux (IMat), Sorbonne University and the French Agence Nationale de la Recherche (ANR), under grant

ANR-18-CE0-0013-02. We would also like to thank several instrumentation facilities located at L'Institut de Minéralogie, de Physique des Matériaux et de Cosmochimie (IMPMC, Paris, France) that enabled streamlines measurement and analysis of datasets presented in this work: Maxime Guillaumet and Keevin Béneut for Spectroscopy platform; Imène Esteve, Stéphanie Delbrel and Béatrice Doisneau for SEM support; Ludovic Delbes and Benoît Baptiste for X-ray diffraction facility; and Cynthia Travert and Feriel Skouri-Panet for GEMME (geomicrobiology) facility. We thank Laure Cordier at Institut de Physique du Globe de Paris (IPGP, Paris, France) for ICP-OES analysis. We thank Pierre Beck at Université Grenoble-Alpes (France) for near-IR analysis and Xavier Carrier from Laboratoire de Réactivité de Surface (Sorbonne University, Paris, France) for TGA-MS analysis. Lastly, we thank the two anonymous reviewers for their constructive feedbacks.

References

(1) Addadi, B. L.; Raz, S.; Weiner, S. Taking Advantage of Disorder : Amorphous Calcium Carbonate and Its Roles in Biomineralization. *Adv. Mater.* **2003**, No. 12, 959–970.

(2) Weiss, I. M.; Tuross, N.; Addadi, L.; Weiner, S. Mollusc Larval Shell Formation: Amorphous Calcium Carbonate Is a Precursor Phase for Aragonite. *J. Exp. Zool.* **2002**, *293* (5), 478–491.

(3) Politi, Y.; Metzler, R. A.; Abrecht, M.; Gilbert, B.; Wilt, F. H.; Sagi, I.; Addadi, L.; Weiner, S.; Gilbert, P. U. P. A. Transformation Mechanism of Amorphous Calcium. *Proc. Natl. Acad. Sci.* **2008**, *105* (45), 17362–17366.

(4) Politi, Y.; Levi-Kalisman, Y.; Raz, S.; Wilt, F.; Addadi, L.; Weiner, S.; Sagi, I. Structural Characterization of the Transient Amorphous Calcium Carbonate Precursor Phase in Sea Urchin Embryos. *Adv. Funct. Mater.* **2006**, *16* (10), 1289–1298.

(5) Politi, Y.; Arad, T.; Klein, E.; Weiner, S.; Addadi, L. Sea Urchin Spine Calcite Forms via a Transient Amorphous Calcium Carbonate Phase. *Science.* **2004**, *306* (5699), 1161–1164.

(6) Aizenberg, J.; Lambert, G.; Weiner, S.; Addadi, L. Factors Involved in the Formation of Amorphous and Crystalline Calcium Carbonate: A Study of an Ascidian Skeleton. *J. Am. Chem. Soc.* **2002**, *124* (1), 32–39.

(7) Salman, V.; Yang, T.; Berben, T.; Klein, F.; Angert, E.; Teske, A. Calcite-Accumulating

Large Sulfur Bacteria of the Genus Achromatium in Sippewissett Salt Marsh. **2015**, 2503–2514.

(8) Monteil, C. L.; Benzerara, K.; Menguy, N.; Bidaud, C. C.; Michot-Achdjian, E.; Bolzoni, R.; Mathon, F. P.; Coutaud, M.; Alonso, B.; Garau, C.; et al. Intracellular Amorphous Ca-Carbonate and Magnetite Biomineralization by a Magnetotactic Bacterium Affiliated to the Alphaproteobacteria. *ISME J.* **2021**, *15* (1).

(9) Couradeau, E.; Benzerara, K.; Gérard, E.; Moreira, D.; Bernard, S.; Brown, G. E. J.; López-García, P. An Early-Branching Microbialite Cyanobacterium Forms Intracellular Carbonates. *Sci* **2012**, *336*, 459–462.

(10) Benzerara, K.; Skouri-Panet, F.; Li, J.; Ferard, C.; Gugger, M.; Laurent, T.; Couradeau, E.; Ragon, M.; Cosmidis, J.; Menguy, N.; et al. Intracellular Ca-Carbonate Biomineralization Is Widespread in Cyanobacteria. *Proc. Natl. Acad. Sci.* **2014**, *111* (30), 10933–10938.

(11) De Wever, A.; Benzerara, K.; Gugger, M.; Coutaud, M.; Caumes, G.; Poinsot, M.; Skouri-Panet, F.; Laurent, T.; Duprat, E.; Gugger, M. Evidence of High Ca Uptake by Cyanobacteria Forming Intracellular CaCO3 and Impact on Their Growth. *Geobiology* **2019**, *17* (6), 1–15.

(12) Cosmidis, J.; Benzerara, K. Why Do Microbes Make Minerals ? *Comptes Rendus Géoscience Planète* **2022**, 0–39.

(13) Mehta, N.; Benzerara, K.; Kocar, B. D.; Chapon, V. Sequestration of Radionuclides Radium-226 and Strontium-90 by Cyanobacteria Forming Intracellular Calcium

552 Carbonates. *Environ. Sci. Technol.* **2019**, *53* (21), 12639–12647.

553 (14) Bradley, J. A.; Daille, L. K.; Trivedi, C. B.; Bojanowski, C. L.; Stamps, B. W.; Stevenson,
554 B. S.; Nunn, H. S.; Johnson, H. A.; Loyd, S. J.; Berelson, W. M.; et al. Carbonate-Rich
555 Dendrolitic Cones: Insights into a Modern Analog for Incipient Microbialite Formation,
556 Little Hot Creek, Long Valley Caldera, California. *npj Biofilms Microbiomes* **2017**, *3* (1).

557 (15) Amarouche-Yala, S.; Benouadah, A.; El Ouahab Bentabet, A.; López-García, P.
558 Morphological and Phylogenetic Diversity of Thermophilic Cyanobacteria in Algerian
559 Hot Springs. *Extremophiles* **2014**, *18* (6), 1035–1047.

560 (16) Couradeau, E.; Benzerara, K.; Gérard, E.; Moreira, D.; Bernard, S.; López-García3, G. E.
561 B. J. P. An Early-Branching Microbialite Cyanobacterium Forms Intracellular Carbonates.
562 *Science.* **2012**, *336*, 459–462.

563 (17) Head, I. M.; Gray, N. D.; Howarth, R.; Pickup, R. W.; Clarke, K. J.; Jones, J. G.
564 Achromatium Oxaliferum Understanding the Unmistakable. In *Advances in Microbial*
565 *Ecology*; Schink, B., Ed.; Springer US: Boston, MA, 2000; pp 1–40.

566 (18) Hodson, M. E.; Benning, L. G.; Demarchi, B.; Penkman, K. E. H.; Rodriguez-Blanco, J.
567 D.; Schofield, P. F.; Versteegh, E. A. A. Biomineralisation by Earthworms - An
568 Investigation into the Stability and Distribution of Amorphous Calcium Carbonate.
569 *Geochem. Trans.* **2015**, *16* (1).

570 (19) Stephens, C. J.; Ladden, S. F.; Meldrum, F. C.; Christenson, H. K. Biomineralization:
571 Amorphous Calcium Carbonate Is Stabilized in Confinement. *Adv. Funct. Mater.* **2010**, *20*
572 (13), n/a-n/a.

(20) Loste, E.; Wilson, R. M.; Seshadri, R.; Meldrum, F. C. The Role of Magnesium in Stabilising Amorphous Calcium Carbonate and Controlling Calcite Morphologies. *J. Cryst. Growth* **2003**, *254* (1–2), 206–218.

(21) Liu, Z.; Zhang, Z.; Wang, Z.; Jin, B.; Li, D.; Tao, J.; Tang, R.; de Yoreo, J. J. Shape-Preserving Amorphous-to-Crystalline Transformation of CaCO3 Revealed by in Situ TEM. *Proc. Natl. Acad. Sci. U. S. A.* **2020**, *117* (7), 3397–3404.

(22) Cavanaugh, J.; Whittaker, M. L.; Joester, D. Crystallization Kinetics of Amorphous Calcium Carbonate in Confinement. *Chem. Sci.* **2019**, 5039–5043.

(23) Li, J.; Margaret Oliver, I.; Cam, N.; Boudier, T.; Blondeau, M.; Leroy, E.; Cosmidis, J.; Skouri-Panet, F.; Guigner, J.-M.; Férard, C.; et al. Biomineralization Patterns of Intracellular Carbonatogenesis in Cyanobacteria: Molecular Hypotheses. *Minerals* **2016**, *6* (1), 10.

(24) Benzerara, K.; Bolzoni, R.; Monteil, C.; Beyssac, O.; Forni, O.; Alonso, B.; Asta, M. P.; Lefevre, C. The Gammaproteobacterium Achromatium Forms Intracellular Amorphous Calcium Carbonate and Not (Crystalline) Calcite. *Geobiology* **2021**, *19* (2), 199–213.

(25) Elderfield, H. The Application of Infra-Red Absorption Spectroscopy to Carbonate Mineralogy. **1967**, *9*, 5–21.

(26) Vagenas, N. V; Gatsouli, A.; Kontoyannis, C. G. Quantitative Analysis of Synthetic Calcium Carbonate Polymorphs Using FT-IR Spectroscopy. *Talanta* **2003**, *59*, 831–836.

(27) Blue, C. R.; Dove, P. M. ScienceDirect Chemical Controls on the Magnesium Content of

593 Amorphous Calcium Carbonate. *Geochim. Cosmochim. Acta* **2015**, *148*, 23–33.

594 (28) Konrad, F.; Purgstaller, B.; Gallien, F.; Mavromatis, V.; Gane, P.; Dietzel, M. Influence of
595 Aqueous Mg Concentration on the Transformation of Amorphous Calcium Carbonate. *J.*
596 *Cryst. Growth* **2018**, *498* (April), 381–390.

597 (29) Beniash, E.; Aizenberg, J.; Addadi, L.; Weiner, S. Amorphous Calcium Carbonate
598 Transforms into Calcite during Sea Urchin Larval Spicule Growth. *Proc. R. Soc. B Biol.*
599 *Sci.* **1997**, *264* (1380), 461–465.

600 (30) Farhadi Khouzani, M.; Chevrier, D. M.; Güttlein, P.; Hauser, K.; Zhang, P.; Hedin, N.;
601 Gebauer, D. Disordered Amorphous Calcium Carbonate from Direct Precipitation.
602 *CrystEngComm* **2015**, *17* (26), 4842–4849.

603 (31) Bots, P.; Benning, L. G.; Rodriguez-Blanco, J. D.; Roncal-Herrero, T.; Shaw, S.
604 Mechanistic Insights into the Crystallization of Amorphous Calcium Carbonate (ACC).
605 *Cryst. Growth Des.* **2012**, *12* (7), 3806–3814.

606 (32) Rodriguez-Blanco, J. D.; Shaw, S.; Benning, L. G. The Kinetics and Mechanisms of
607 Amorphous Calcium Carbonate (ACC) Crystallization to Calcite, via Vaterite. *Nanoscale*
608 **2011**, *3* (1), 265–271.

609 (33) Hodson, M. E.; Benning, L. G.; Cinquc, G.; Dcmarchi, B.; Froglcy, M.; Penkman, K. E.
610 H.; Rodriguez-Bianco, J. D.; Schofield, P. F.; Versteegh, E. A. A.; Wehbe, K.
611 Synchrotron-Based Micro Fourier Transform Infrared Mapping to Investigate the Spatial
612 Distribution of Amorphous and Crystalline Calcium Carbonate in Earthworm-Secreted
613 Calcium Carbonate Balls. *Spectrosc. Eur.* **2016**, *28* (3), 3–6.

(34) Foran, E.; Weiner, S.; Fine, M. Biogenic Fish-Gut Calcium Carbonate Is a Stable Amorphous Phase in the Gilt-Head Seabream, Sparus Aurata. *Sci. Rep.* **2013**, *3*, 1–5.

(35) Gago-Duport, L.; Briones, M. J. I.; Rodríguez, J. B.; Covelo, B. Amorphous Calcium Carbonate Biomineralization in the Earthworm's Calciferous Gland: Pathways to the Formation of Crystalline Phases. *J. Struct. Biol.* **2008**, *162* (3), 422–435.

(36) Campbell, S.; Poduska, K. M. Incorporating Far-Infrared Data into Carbonate Mineral Analyses. *Minerals* **2020**.

(37) Brusentsova, T.; Peale, R.; Maukonen, D.; Harlow, G.; Bosenberg, J.; Ebel, D. Far Infrared Spectroscopy of Carbonate Minerals. *Am. Mineral.* **2010**, *95* (1967), 1515–1522.

(38) Enyedi, N. T.; Makk, J.; Kótai, L.; Berényi, B.; Klébert, S.; Sebestyén, Z.; Molnár, Z.; Borsodi, A. K.; Leél-Őssy, S.; Demény, A.; et al. Cave Bacteria-Induced Amorphous Calcium Carbonate Formation. *Sci. Rep.* **2020**, *10* (1), 1–12.

(39) Liu, R.; Huang, S.; Zhang, X.; Song, Y.; He, G.; Wang, Z.; Lian, B. Bio-Mineralisation, Characterization, and Stability of Calcium Carbonate Containing Organic Matter. *RSC Adv.* **2021**, *11* (24), 14415–14425.

(40) Guido, A.; Mastandrea, A.; Russo, F. Biotic vs Abiotic Carbonates: Characterisation of the Fossil Organic Matter with Fourier-Transform Infrared (FT-IR) Spectroscopy. *Boll. della Soc. Paleontol. Ital.* **2013**, *52* (1), 63–70.

(41) Dean, A. P.; Martin, M. C.; Sigee, D. C. Resolution of Codominant Phytoplankton Species in a Eutrophic Lake Using Synchrotron-Based Fourier Transform Infrared Spectroscopy.

Phycologia **2007**, *46* (2), 151–159.

(42) Von Euw, S.; Azaïs, T.; Manichev, V.; Laurent, G.; Pehau-Arnaudet, G.; Rivers, M.; Murali, N.; Kelly, D. J.; Falkowski, P. G. Solid-State Phase Transformation and Self-Assembly of Amorphous Nanoparticles into Higher-Order Mineral Structures. *J. Am. Chem. Soc.* **2020**, *142* (29), 12811–12825.

(43) Stanier, R. Y.; Deruelles, J.; Rippka, R.; Herdman, M.; Waterbury, J. B. Generic Assignments, Strain Histories and Properties of Pure Cultures of Cyanobacteria. *Microbiology* **1979**, *111* (1), 1–61.

(44) Potin, S.; Brissaud, O.; Beck, P.; Schmitt, B.; Magnard, Y.; Correia, J.-J.; Rabou, P.; Jocou, L. SHADOWS: A Spectro-Gonio Radiometer for Bidirectional Reflectance Studies of Dark Meteorites and Terrestrial Analogs: Design, Calibrations, and Performances on Challenging Surfaces. *Appl. Opt.* **2018**, *57* (28), 8279.

(45) Whalley, E.; Bertie, J. E. The Far Infrared Spectrum and Long-Range Forces in Ice. *J. Colloid Interface Sci.* **1967**, *25* (2), 161–165.

(46) Cloutis, E. A.; Grasby, S. E.; Last, W. M.; Léveillé, R.; Osinski, G. R.; Sherriff, B. L. Spectral Reflectance Properties of Carbonates from Terrestrial Analogue Environments: Implications for Mars. *Planet. Space Sci.* **2010**, *58* (4), 522–537.

(47) Hunt, G. R.; Ashley, R. P. Altered Rock Spectra in the Visible and near Infrared. *Econ. Geol.* **1979**, *74*, 1613–1629.

(48) Gaffey, S. J. Spectral Reflectance of Carbonate Minerals in the Visible and near Infrared

(0.35-2.55 Microns); Calcite, Aragonite, and Dolomite. *Am. Mineral.* **1986**, *71* (1–2), 151–162.

(49) Harner, P. L.; Gilmore, M. S. Visible-near Infrared Spectra of Hydrous Carbonates, with Implications for the Detection of Carbonates in Hyperspectral Data of Mars. *Icarus* **2015**, *250*, 204–214.

(50) Benning, L. G.; Phoenix, V. R.; Yee, N.; Tobin, M. J. Molecular Characterization of Cyanobacterial Silicification Using Synchrotron Infrared Micro-Spectroscopy. *Geochim. Cosmochim. Acta* **2004**, *68* (4), 729–741.

(51) Murdock, J. N.; Wetzel, D. L. FT-IR Microspectroscopy Enhances Biological and Ecological Analysis of Algae. *Appl. Spectrosc. Rev.* **2009**, *44* (4), 335–361.

(52) Kansiz, M.; Heraud, P.; Wood, B.; Burden, F.; Beardall, J.; Mcnaughton, D. Fourier Transform Infrared Microspectroscopy and Chemometrics as a Tool for the Discrimination of Cyanobacterial Strains. **1999**, *52*.

(53) Ftir, B. F. I.; Özer, T.; Yalçın, D.; Erkaya, I. A.; Udoh, A. U. Identification and Characterization of Some Species of Cyanobacteria , Identification and Characterization of Some Species of Cyanobacteria , Chlorophyta and BacillariophytaUsing Fourier-Transform Infrared (FTIR) Spectroscopy. **2019**, No. January.

(54) Stuart, B. *IR Spectroscopy-Fundamentals*; Wiley.

(55) Vaidyanathan, S.; Macaloney, G.; McNeil, B. Fundamental Investigations on the Near-Infrared Spectra of Microbial Biomass as Applicable to Bioprocess Monitoring. *Analyst*

1999, *124* (2), 157–162.

(56) Craven, S. M.; Bentley, F. F. Far Infrared Group Frequencies . II . Primary Amines. *Appl. Spectrosc.* **1972**, *26* (4).

(57) Fateley, G. W.; Miller, F. A. Torsional Frequencies in the Far Infrared-II Molecules with Two or Three Methyl Rotors. *Spectrochim. Acta - Part A Mol. Biomol. Spectrosc.* **1962**.

(58) Fischer, B. M.; Walther, M.; Jepsen, P. U. Far-Infrared Vibrational Modes of DNA Components Studied by Terahertz Time-Domain Spectroscopy. *Phys. Med. Biol.* **2002**.

(59) Aizenberg, J.; Weiner, S.; Addadi, L. Coexistence of Amorphous and Crystalline Calcium Carbonate in Skeletal Tissues. *Connect. Tissue Res.* **2003**, *44* (SUPPL. 1), 20–25.

(60) Burgula, Y.; Khali, D.; Kim, S.; Krishnan, S. S.; Cousin, M. A.; Gore, J. P.; Reuhs, B. L.; Mauer, L. J. Review of Mid-Infrared Fourier Transform-Infrared Spectroscopy Applications for Bacterial Detection. *J. Rapid Methods Autom. Microbiol.* **2007**, *15* (2), 146–175.

(61) Naumann, D. FT-Infrared and FT-Raman Spectroscopy in Biomedical Research. *Appl. Spectrosc. Rev.* **2001**, *36* (2–3), 239.

(62) Jiang, W.; Saxena, A.; Song, B.; Ward, B. B.; Beveridge, T. J.; Myneni, S. C. B. Elucidation of Functional Groups on Gram-Positive and Gram-Negative Bacterial Surfaces Using Infrared Spectroscopy. *Langmuir* **2004**, *20* (26), 11433–11442.

(63) Huisman, J.; Codd, G. A.; Paerl, H. W.; Ibelings, B. W.; Verspagen, J. M. H.; Visser, P. M. Cyanobacterial Blooms. *Nat. Rev. Microbiol.* **2018**, *16* (8), 471–483.

(64) Inaba, N.; Kodama, I.; Nagai, S.; Shiraishi, T.; Matsuno, K.; Yamaguchi, A.; Imai, I. Distribution of Harmful Algal Growth-Limiting Bacteria on Artificially Introduced Ulva and Natural Macroalgal Beds. *Appl. Sci.* **2020**, *10* (16), 1–16.

(65) Paerl, H. W.; Otten, T. G. Harmful Cyanobacterial Blooms: Causes, Consequences, and Controls. *Microb. Ecol.* **2013**, *65* (4), 995–1010.

(66) O'Neil, J. M.; Davis, T. W.; Burford, M. A.; Gobler, C. J. The Rise of Harmful Cyanobacteria Blooms: The Potential Roles of Eutrophication and Climate Change. *Harmful Algae* **2012**, *14*, 313–334.

(67) Garand, E.; Wende, T.; Goebbert, D. J.; Bergmann, R.; Meijer, G.; Neumark, D. M.; Asmis, K. R.; Science, C.; Di, V.; Berkeley, L. Infrared Spectroscopy of Hydrated Bicarbonate Anion. *JACS* **2010**, No. 4, 849–856.

(68) Badger, M. R.; Andrews, T. J. Photosynthesis and Inorganic Carbon Usage by the Marine I-Fl. *Plant Physiol.* **1982**, *70*, 517–523.

(69) Garand, E.; Wende, T.; Goebbert, D. J.; Bergmann, R.; Meijer, G.; Neumark, D. M.; Asmis, K. R.; Science, C.; Di, V.; Berkeley, L. Infrared Spectroscopy of Hydrated Bicarbonate Anion. **2010**, No. 4, 849–856.

(70) Shutova, V. V; Tyutyaev, E. V; Churin, A. A.; Ponomarev, V. Y. CELL BIOPHYSICS IR and Raman Spectroscopy in the Study of Carotenoids of Cladophora Rivularis Algae. **2016**, *61* (4), 601–605.

(71) Cojoc, L. R.; Enache, M. I.; Neagu, S. E.; Lungulescu, M.; Setnescu, R.; Ruginescu, R.;

Gomoiu, I. Carotenoids Produced by Halophilic Bacterial Strains on Mural Paintings and Laboratory Conditions. *FEMS Microbiol. Lett.* **2019**.

(72) Wang, R.; Ma, Y.; Zhang, D.; Li, W. Analysis of Polyphosphate during the Enhanced Biological Phosphorus Removal Process Using Fourier Transform Infrared (FTIR) Spectroscopy. *E3S Web Conf. EDP Sci.* **2020**, *7*.

(73) Stewart, J. L. The IR Spectrum of the Nitrate Ion in Various Crystalline Enviornments, 1965.

(74) Stehfest, K.; Toepel, J.; Wilhelm, C. The Application of Micro-FTIR Spectroscopy to Analyze Nutrient Stress-Related Changes in Biomass Composition of Phytoplankton Algae. **2005**, *43*, 717–726.

(75) Benning, L. G.; Phoenix, V. R.; Yee, N.; Konhauser, K. O. The Dynamics of Cyanobacterial Silicification: An Infrared Micro-Spectroscopic Investigation. *Geochim. Cosmochim. Acta* **2004**, *68* (4), 743–757.

(76) Baker, M. J.; Trevisan, J.; Bassan, P.; Bhargava, R.; Butler, H. J. Using Fourier Transform IR Spectroscopy to Analyze Biological Materials. **2015**, *9* (8), 1771–1791.